Macroscopic self-oscillations and aging transition in a network of synaptically coupled quadratic integrate-and-fire neurons

Irmantas Ratas[1] and Kestutis Pyragas[1,2]
[1]*Center for Physical Sciences and Technology, LT-10257 Vilnius, Lithuania*
[2]*Department of Theoretical Physics, Faculty of Physics, Vilnius University, LT-10222 Vilnius, Lithuania*
(Received 13 June 2016; published 19 September 2016)

We analyze the dynamics of a large network of coupled quadratic integrate-and-fire neurons, which represent the canonical model for class I neurons near the spiking threshold. The network is heterogeneous in that it includes both inherently spiking and excitable neurons. The coupling is global via synapses that take into account the finite width of synaptic pulses. Using a recently developed reduction method based on the Lorentzian ansatz, we derive a closed system of equations for the neuron's firing rate and the mean membrane potential, which are exact in the infinite-size limit. The bifurcation analysis of the reduced equations reveals a rich scenario of asymptotic behavior, the most interesting of which is the macroscopic limit-cycle oscillations. It is shown that the finite width of synaptic pulses is a necessary condition for the existence of such oscillations. The robustness of the oscillations against aging damage, which transforms spiking neurons into nonspiking neurons, is analyzed. The validity of the reduced equations is confirmed by comparing their solutions with the solutions of microscopic equations for the finite-size networks.

DOI: 10.1103/PhysRevE.94.032215

I. INTRODUCTION

Complex systems composed of a large number of interacting nonlinear dynamical elements are ubiquitous in nature. Synchronization and other collective effects in such systems is a pervasive topic in physics, chemistry, biology, social networks, and technological applications [1–4]. Example systems include Josephson junction arrays [5], power grids [6], cardiac pacemaker cells [7], and neurons in human brain [8], among others.

The pioneering theoretical work on the collective behavior of limit-cycle oscillators was done by Winfree [9]. Using a mean-field model of coupled phase oscillators with distributed natural frequencies, he discovered that collective synchronization is a threshold phenomenon analogous to a phase transition. The theory was further advanced by Kuramoto [10], who proposed an analytically tractable model of phase oscillators with an all-to-all sinusoidal coupling. The Kuramoto model and various of its modifications were extensively studied during the past two decades [2–4]. A major breakthrough in these studies was achieved by Ott and Antonsen [11] a few years ago. They showed that, in the infinite-size (thermodynamic) limit, the Kuramoto-type models display low-dimensional dynamics and derived an explicit finite set of nonlinear ordinary differential equations for the macroscopic evolution of the system. Later this idea was elaborated on in various modifications of phase oscillator networks [12–17] and adopted for globally coupled networks of theta neurons [18–20], networks of theta neurons with spatially dependent coupling [21], networks incorporating gap junctions [22], and a pulse-coupled Winfree model [23].

Recently, Montbrió, Pazó, and Roxin [24] proposed an alternative approach to reduce a set of microscopic equations for a particular class of neuronal systems. They considered a heterogeneous network of all-to-all pulselike coupled quadratic integrate-and-fire (QIF) neurons with some part of them being in a spiking regime and another part in an excitable (nonspiking) regime. The authors found out that in the thermodynamic limit the continuity equation can be solved by the Lorentzian ansatz (LA). As a result, they derived the closed system of two ordinary differential equations for biophysically relevant macroscopic quantities: the firing rate and the mean membrane potential. They also demonstrated the relation of the LA with the Ott-Antonsen ansatz [11].

In Ref. [24], the consideration was restricted to a relatively simple model of neuronal interaction. It was assumed that at each moment when a particular neuron fires, an interaction current generated in postsynaptic neurons can be approximated by the Dirac δ function. Here we consider a more realistic synaptic coupling between QIF neurons that takes into account the finite width of synaptic pulses and other peculiarities of a realistic synapse. We show that the LA theory is suitable for this more complicated case as well and derive the reduced equations that result in a much richer scenario of dynamical behavior as compared to that of Ref. [24]. We have found out that the finite width of synaptic pulses is a crucial factor for the emergence of macroscopic self-sustained oscillations of the firing rate and mean membrane potential.

In this paper, we also analyze the robustness of the macroscopic self-oscillations against local damage that transforms spiking neurons into nonspiking neurons. When the proportion of the inactive elements in a network exceeds some threshold value, the macroscopic oscillations stop and this may cause a loss of a physiological function of the network. Such a phenomenon is called an aging transition [25]. The analysis of the aging transition [26–31] is important to get more insight into the properties and functions of real populations composed of active and inactive units such as mammalian circadian clocks [32,33] and also be useful in developing a biological pacemaker for heart beat by means of converting excitable heart cells into pacemaker cells by gene transfer [34,35]. Here we use the advantage of the reduced equations for the QIF neurons in order to analyze the dependence of the aging transition on the coupling strength and the width of synaptic pulses.

The paper is organized as follows. In Sec. II, we formulate the problem and describe our model. The reduced equations for the firing rate and mean membrane potential are derived in the thermodynamic limit in Sec. III. Section IV is devoted to the bifurcation analysis of the reduced macroscopic equations. The results are compared with the direct numerical simulations of the microscopic equations. Then, in Sec. V, the robustness of the macroscopic oscillations against the deterioration of the spiking neurons is investigated. Finally, in Sec. VI, we conclude this paper by discussing our results.

II. PROBLEM FORMULATION AND MODEL DESCRIPTION

We consider a heterogeneous population of N all-to-all synaptically coupled quadratic integrate-and-fire neurons. The microscopic state of the system is defined by neurons' membrane potentials $\{V_j\}_{j=1,\ldots,N}$, which satisfy the following set of equations [8]:

$$\dot{V}_j = V_j^2 + \eta_j + I_j^{\mathrm{syn}}. \tag{1}$$

Here the constants η_j specify the behavior of individual neurons, while I_j^{syn} stands for the synaptic current. Each moment the membrane potential V_j reaches the peak value V_{peak} its voltage is reset to the value V_{reset}. To treat the system analytically, we assume $V_{\mathrm{peak}} = -V_{\mathrm{reset}} \to \infty$.

The isolated ($I_j^{\mathrm{syn}} = 0$) QIF neuron is the canonical model for the class I neurons near the spiking threshold. The spiking instability in such neurons appears through a saddle-node bifurcation on an invariant curve (SNIC), in which a pair of fixed points on a closed curve coalesce to disappear, converting the curve to a periodic orbit. A remarkable feature of a system following this scenario is that it exhibits excitability before the bifurcation. In the QIF neuron, this scenario is provided by the bifurcation parameter η_j. For $\eta_j < 0$, the neuron is in an excitable regime and for $\eta_j > 0$ it is in the spiking regime. We assume that the system (1) contains both excitable ($\eta_j < 0$) and spiking neurons ($\eta_j > 0$). Generally, we suppose that the values of the parameters η_j are distributed according to some defined density function $g(\eta)$.

Now we discuss the term I_j^{syn} responsible for synaptic coupling of neurons. The simplest theoretical model of the synaptic coupling is based on the assumption that the spikes generated by neurons are very short and can be modeled by the Dirac δ function, i.e., the synaptic current can be presented by a sum of δ functions coming from neurons that reached the peak voltage. With such an assumption, the system (1) has been recently analyzed by Montbrió *et al.* [24]. In the thermodynamic limit of a large number of neurons $N \to \infty$, the authors developed a theory based on the Lorentzian ansatz, which allowed them to reduce the system (1) to only two ordinary differential equations for the firing rate and mean membrane potential of the neuronal population. Here we use the LA theory for a more realistic model of synaptic coupling and derive reduced equations that at certain values of the parameters exhibit macroscopic oscillations, which do not exist in the model of Ref. [24]. We also show that our reduced model is suitable for the prediction of aging transition that appears in the system when the proportion of spiking neurons is decreased.

We start our consideration from the standard expression for the synaptic current [8,36]

$$I_j^{\mathrm{syn}} = -(V_j - V_s)\frac{g_s}{N}\sum_{i=1}^{N} w_{ji} s_i, \tag{2}$$

where V_s is the reversal potential of synapse, g_s is the maximal conductance of postsynaptic receptors, and the factor w_{ji} is the measure of the efficacy of the synaptic connection from neuron i to neuron j. An action potential results in an opening of the ion gates in the postsynaptic membrane. The fraction of channels in open state s_i is governed by the equation

$$\dot{s}_i = \alpha\Theta[(V_i - V_{\mathrm{th}})/\sigma](1 - s_i) - \beta s_i, \tag{3}$$

where α, β, σ, and V_{th} are the characteristic parameters of the synapse and $\Theta(V) = [1 + \exp(-V)]^{-1}$ is a sigmoid function. We make the following simplifications. We assume that synaptic dynamics are fast ($\alpha, \beta \gg 1$) so the time derivative in Eq. (3) can be neglected and s_i can be expressed through V_i as $s_i = \alpha\Theta[(V_i - V_{\mathrm{th}})/\sigma]/\{\alpha\Theta[(V_i - V_{\mathrm{th}})/\sigma] + \beta\}$. In addition we suppose that the parameter $\sigma > 0$ is small and the sigmoid function can be approximated by the Heaviside step function $\Theta[(V_i - V_{\mathrm{th}})/\sigma] \approx H(V_i - V_{\mathrm{th}})$, which satisfies $H(V_i - V_{\mathrm{th}}) = 0$ for $V_i \leqslant V_{\mathrm{th}}$ and $H(V_i - V_{\mathrm{th}}) = 1$ for $V_i > V_{\mathrm{th}}$. Then, assuming all-to-all coupling with the coefficients $w_{ji} = 1$, we arrive at the following expression for the synaptic current:

$$I_j^{\mathrm{syn}} = -K(V_j - V_s)S, \tag{4}$$

where

$$S = \frac{1}{N}\sum_{i=1}^{N} H(V_i - V_{\mathrm{th}}), \tag{5}$$

is a synaptic variable that characterizes the mean conductivity of the synapse and $K = g_s\alpha/(\alpha + \beta)$ is the parameter defining the coupling strength. According to Eq. (5), the contribution to the mean conductivity comes only from those neurons whose membrane potential exceeds the threshold value V_{th}. Finally, the microscopic equations of our model reads as follows:

$$\dot{V}_j = V_j^2 + \eta_j - K(V_j - V_s)\frac{1}{N}\sum_{i=1}^{N} H(V_i - V_{\mathrm{th}}). \tag{6}$$

III. THERMODYNAMIC LIMIT $N \to \infty$

To derive macroscopic equations for the ensemble of synaptically coupled neurons (6), we refer to the LA theory developed in Ref. [24]. In the thermodynamic limit $N \to \infty$, we can describe the system by a continuous density function $\rho(V|\eta,t)$, where the product $\rho(V|\eta,t)dV$ defines the fraction of neurons with membrane potential between V and $V + dV$ and parameter η at time t. This function satisfies the normalization condition

$$\int_{-\infty}^{+\infty}\int_{-\infty}^{+\infty} \rho(V|\eta,t)g(\eta)dV\,d\eta = 1. \tag{7}$$

Since oscillators are conserved, the density $\rho(V|\eta,t)$ obeys the continuity equation

$$\frac{\partial}{\partial t}\rho = -\frac{\partial}{\partial V}[\rho\{V^2 + \eta - K(V - V_s)S\}]. \tag{8}$$

A remarkable feature of this equation is that its stationary solution satisfies the Lorentzian function, i.e., $\rho_0(V|\eta) \propto [(V - KS/2)^2 + \eta + KV_sS - (KS/2)^2]^{-1}$. Based on this observation, the authors of Ref. [24] assumed that solutions of Eq. (8) generically (for any initial conditions) converge to a Lorentzian-shaped function,

$$\rho(V|\eta,t) = \frac{1}{\pi}\frac{x(\eta,t)}{[V - y(\eta,t)]^2 + x(\eta,t)^2}, \tag{9}$$

with two time-dependent parameters, $x(\eta,t)$ and $y(\eta,t)$, which define the half-width and the center of the distribution. These two parameters characterize all relevant dynamics of the system in a reduced subspace. The validity of this assumption is confirmed [24] by its relation with Ott-Antonsen ansatz [11].

The parameters $x(\eta,t)$ and $y(\eta,t)$ of the Lorentzian function have clear physical meanings. For a fixed η, the neurons firing rate is related to the Lorentzian half-width by

$$x(\eta,t) = \pi r(\eta,t). \tag{10}$$

This relation is obtained by estimating the probability flux at $V \to +\infty$, which by definition is the firing rate: $r(\eta,t) = \rho(V \to \infty|\eta,t)\dot{V}(V \to \infty|\eta,t)$. The total firing rate $r(t)$ is obtained via integration of the product $r(\eta,t)g(\eta)$ over η:

$$r(t) = \frac{1}{\pi}\int_{-\infty}^{+\infty} x(\eta,t)g(\eta)d\eta. \tag{11}$$

Furthermore, by defining the integral

$$y(\eta,t) = \text{p.v.}\int_{-\infty}^{+\infty} \rho(V|\eta,t)V dV \tag{12}$$

as the Cauchy principal value [$\text{p.v.}\int_{-\infty}^{+\infty} f(x)dx = \lim_{R\to\infty}\int_{-R}^{+R} f(x)dx$], we can see that the mean membrane potential is equal to

$$v(t) = \int_{-\infty}^{+\infty} y(\eta,t)g(\eta)d\eta. \tag{13}$$

In the thermodynamic limit, the sum in the definition (5) of the synaptic variable $S = S(t)$ should be replaced by the integral

$$S(t) = \int_{-\infty}^{+\infty} g(\eta)\int_{-\infty}^{+\infty} \rho(V|\eta,t)H(V - V_{\text{th}})dV d\eta. \tag{14}$$

The integration over the V variable can be performed analytically and we get

$$S(t) = \frac{1}{\pi}\int_{-\infty}^{+\infty}\left\{\frac{\pi}{2} - \arctan\left[\frac{V_{\text{th}} - y(\eta,t)}{x(\eta,t)}\right]\right\}g(\eta)d\eta. \tag{15}$$

Substituting the LA (9) into the continuity equation (8), one can derive a system of two differential equations for $x(\eta,t)$ and $y(\eta,t)$,

$$\dot{x}(\eta,t) = 2x(\eta,t)y(\eta,t) - Kx(\eta,t)S(t), \tag{16a}$$

$$\dot{y}(\eta,t) = \eta - x^2(\eta,t) + y^2(\eta,t) - KS(t)[y(\eta,t) - V_s], \tag{16b}$$

which for the complex variable $w(\eta,t) \equiv x(\eta,t) + iy(\eta,t)$ can be written as

$$\dot{w}(\eta,t) = i[\eta - w^2(\eta,t) + K(iw(\eta,t) + V_s)S(t)]. \tag{17}$$

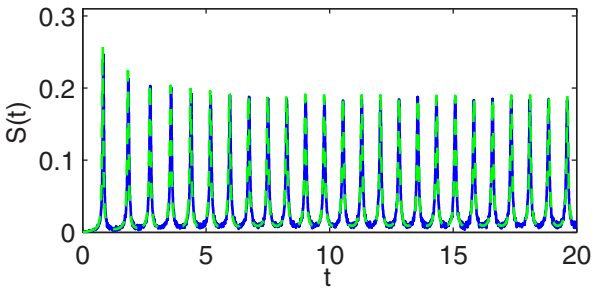

FIG. 1. Comparison of dynamics of the synaptic variable $S(t)$ estimated from the microscopic model (5) and (6) (blue solid curve) and the reduced system (20) and (21) (green dashed curve). Parameters are $N = 10\,000$, $\Delta = 1$, $\bar{\eta} = 0$, $V_{\text{th}} = 50$, $V_s = 75$, and $K = 20$.

Further simplification can be gained by choosing the density distribution of the η parameter in the Lorentzian function form

$$g(\eta) = \frac{1}{\pi}\frac{\Delta}{(\eta - \bar{\eta})^2 + \Delta^2}, \tag{18}$$

where Δ and $\bar{\eta}$ define the width and the center of the distribution, respectively. The form (18) allows us to solve the η integrals in Eqs. (11), (13), and (15). This is done by making an analytical continuation of $w(\eta,t)$ from real η into complex η plane and closing the integration contour in the lower half plane [24]. The values of these integrals are determined by the pole $\eta = \bar{\eta} - i\Delta$ of $g(\eta)$ in the lower half η plane and thus we obtain an explicit relation of the firing rate and the mean membrane potential with the complex variable w,

$$\pi r(t) + iv(t) = w(\bar{\eta} - i\Delta, t), \tag{19}$$

as well as an explicit expression for the integral (15),

$$S(t) = \frac{1}{\pi}\left\{\frac{\pi}{2} - \arctan\left[\frac{V_{\text{th}} - v(t)}{\pi r(t)}\right]\right\}. \tag{20}$$

Putting these results into Eq. (17), i.e., setting $\eta = \bar{\eta} - i\Delta$ and using the relation (19) when separating the real and imaginary parts of Eq. (17), we finally derive the equations for the firing rate and the mean membrane potential,

$$\dot{r} = \Delta/\pi + 2rv - KrS(t), \tag{21a}$$

$$\dot{v} = \bar{\eta} + v^2 - \pi^2r^2 - K(v - V_s)S(t). \tag{21b}$$

These equations together with Eq. (20) form the closed macroscopic model for the network of QIF neurons (6) connected via a realistic synaptic coupling.

The potential of the reduced model (21) to predict the behavior of a large scale network of coupled QIF neurons is demonstrated in Fig. 1. For a fixed values of the parameters $\Delta = 1$, $\bar{\eta} = 0$, $V_{\text{th}} = 50$, $V_s = 75$, and $K = 20$, we compare the dynamics of the synaptic variable $S(t)$ derived from the macroscopic model (20) with that obtained from the microscopic model (6) consisting of $N = 10\,000$ neurons. We see that both solutions are in excellent agreement. This confirms the validity of the above analytical treatment, i.e., the LA theory is valid for the case of more complicated synaptic coupling, as has been considered in Ref. [24]. Remarkably,

here we observe a regime of self-sustained macroscopic oscillations that do not exist in Ref. [24].

Finally, we remark on numerical analysis of the microscopic model. Direct numerical integration of Eqs. (6) is problematic because the membrane potential of the QIF neuron tends to infinity at the moment when the neuron fires. To avoid this problem, we change the variables $V_j = \tan(\theta_j/2)$ to transform the QIF neurons into the theta neurons and then perform the numerical analysis (see Appendix A for details).

IV. BIFURCATION ANALYSIS OF MACROSCOPIC EQUATIONS

The macroscopic model (21) consists of two ordinary differential equations and contains five parameters: Δ, $\bar{\eta}$, K, V_{th}, and V_s. Without loss of generality, we can set $\Delta = 1$ as this parameter can be omitted by an appropriate rescaling of the variables r, v, and t. To further reduce the number of parameters, we consider the limit $V_s \to \infty$ and $K \to 0$ with the product KV_s remaining finite. Then Eqs. (21) can be written as

$$\dot{r} = 1/\pi + 2rv \equiv f(r,v), \tag{22a}$$

$$\dot{v} = \bar{\eta} + v^2 - \pi^2 r^2 + JV_{\text{th}}S(t) \equiv g(r,v), \tag{22b}$$

where a new parameter $J = KV_s/V_{\text{th}}$ defines the strength of synaptic coupling in the simplified model. As a result, we remain with only three independent parameters $\bar{\eta}$, J, and V_{th}. The microscopic Eqs. (6) in this case simplify to

$$\dot{V}_j = V_j^2 + \eta_j + J\frac{V_{\text{th}}}{N}\sum_{i=1}^{N} H(V_i - V_{\text{th}}) \tag{23}$$

and Eqs. (16) for $x(\eta,t)$ and $y(\eta,t)$ read

$$\dot{x}(\eta,t) = 2x(\eta,t)y(\eta,t), \tag{24a}$$

$$\dot{y}(\eta,t) = \eta - x^2(\eta,t) + y^2(\eta,t) + JV_{\text{th}}S(t). \tag{24b}$$

An expression for the synaptic current as described by Eq. (23), which neglects the linear dependence on the membrane potential defined by the factor $V_j - V_s$, is often used in simplified synaptic models. It is a good approximation for small excitatory synapses on a large compartment [37]. In that case, the depolarization of the membrane is small and the difference $V_j - V_s$ is little changed during the excitatory postsynaptic potential. However, if the synapse is located on a thin dendrite, the local membrane potential V_j changes considerably when the synapse is activated. In that case, the original model (6) seems more appropriate.

Below we mainly concentrate on the simplified model (22) as it facilitates the bifurcation analysis of the system. It allows us to derive analytical expressions for bifurcation curves. Remarkably, in Appendix B, we show that the bifurcation diagrams of the simplified system (22) and the original model (21) are qualitatively similar. Another advantage of the simplified model is that both the macroscopic (22) and microscopic (23) equations transform to the corresponding equations of Ref. [24] in the limit $V_{\text{th}} \to \infty$.

Indeed, in this limit, the term $V_{\text{th}}S(t)$ in Eq. (22b) transforms to the firing rate $r(t)$ and the term $V_{\text{th}}H[V_i(t) - V_{\text{th}}]$ in Eq. (23) tends to the Dirac δ function $\delta(t - t_i^s)$, where t_i^s is the moment when the ith neuron fires, i.e., its membrane potential approaches infinity. When the threshold voltage V_{th} is finite, the neurons interact via pulses of finite width Δt. For large V_{th}, there is a simple relation between the pulse width and the threshold voltage. Close to the firing moment t_i^s of the ith neuron, its dynamics can be approximated by the differential equation $\dot{V}_i = V_i^2$. The solution of this equation is $V_i(t) = (t_i^s - t)^{-1}$ and thus the term $V_{\text{th}}H[V_i(t) - V_{\text{th}}]$ generates a rectangular pulse located at the left-hand side of the point t_i^s. The width of the pulse is $\Delta t = 1/V_{\text{th}}$ and its height is V_{th} so the area under the pulse is equal to unity for any large V_{th}. Thus we can analyze how the dynamical properties of the model [24] change when one takes into account the finite width of synaptic pulses. We emphasize that for large V_{th} an area under synaptic pulses generated by the term $V_{\text{th}}S(t)$ is independent of V_{th}. This is why we introduced the factor V_{th} in the expression of synaptic current in Eqs. (22b) and (23).

In Fig. 2, we show the bifurcation diagram of the macroscopic model (22) in the plane of the parameters $(\bar{\eta}, J)$ for the fixed threshold voltage $V_{\text{th}} = 50$. There are six regions in the $(\bar{\eta}, J)$ plane with different characteristic behavior of the system illustrated by the phase portraits shown in the right-hand side of the figure. In regions (I), (III), and (IV), the system has a single fixed point. In region (I), there is a stable node, while in region (IV) there is a stable focus. Region (III) is characterized by the presence of an unstable focus and a stable limit cycle that produces macroscopic oscillations of the firing rate and the mean membrane potential. The remaining regions (II), (V), and (VI) are characterized by the presence of three fixed points. In region (II), only one fixed point is stable, while the region (V) is characterized by bistability—there are a stable node and a stable focus separated by a saddle fixed point. Region (VI) is also characterized by bistability, but here we have coexisting a stable fixed point and a stable limit cycle, which are again separated by a saddle fixed point. Comparing this bifurcation diagram with that presented in Fig. 1 of Ref. [24], we see that the finite width of synaptic pulses has produced three additional regions in the bifurcation diagram: (II), (III), and (VI). They are related with the appearance of the macroscopic limit-cycle oscillations, which do not exist in the case of synaptic coupling described by zero width pulses.

Note that macroscopic limit-cycle oscillations have been observed in a model of theta neurons coupled via pulses of finite width in Ref. [18]. However, the form of the coupling term in that model is not physically motivated. It is a purely mathematical assumption that does not reflect the main properties of the synaptic coupling even qualitatively, e.g., according to the model, the neurons in a post-reset state give a contribution into synaptic current.

Below we discuss bifurcations that appear in the plane of parameters $(\bar{\eta}, J)$ in more detail and verify their existence by numerical simulations of the microscopic model (23). First, we consider the local bifurcations, which can be analyzed entirely through changes in the local stability properties of fixed points. The coordinates (r_e, v_e) of the fixed points in the plane of variables (r,v) are obtained by solution of the

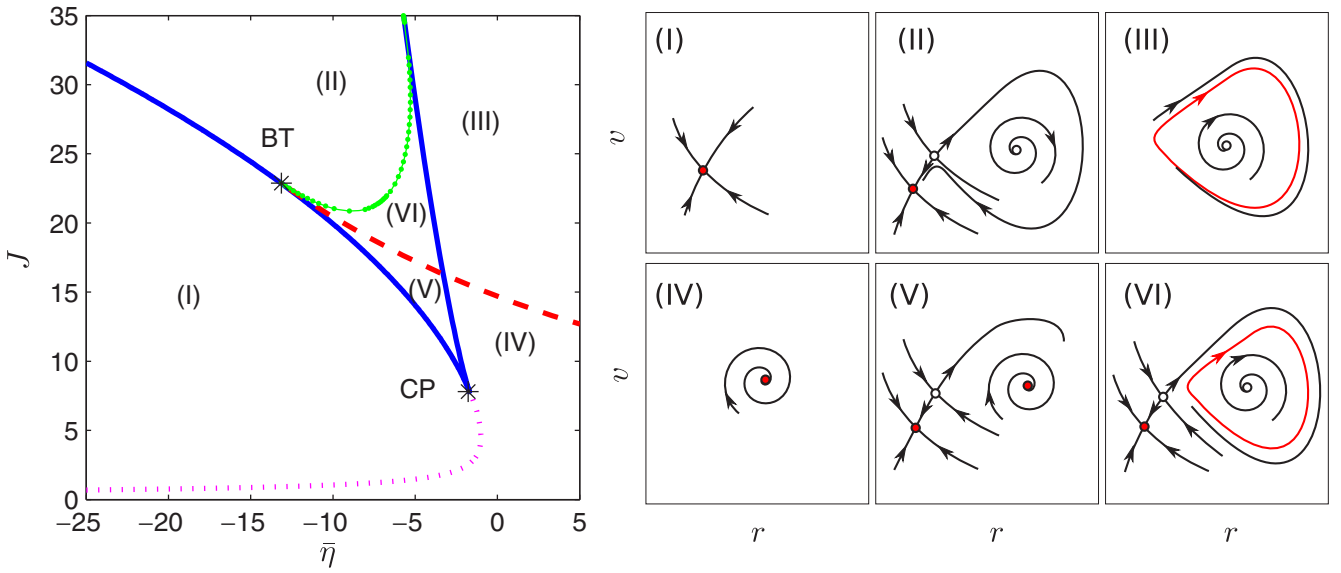

FIG. 2. Two-parameter bifurcation diagram of the macroscopic model (22). The bifurcation in the parameter space $(\bar{\eta}, J)$ for the fixed parameter $V_{\text{th}} = 50$. The blue solid curve shows the saddle-node bifurcation, the red dashed curve the Andronov-Hopf bifurcation, and the green connected points the homoclinic bifurcation. The dotted magenta curve separates the regions with a stable node and a stable focus. The points BT and CP denote the Bogdanov-Takens and the cusp bifurcations, respectively. The regions marked by Roman numerals correspond to the following set of fixed points and invariant curves: (I) a stable node; (II) a saddle, an unstable focus, and an stable node; (III) an unstable focus and a stable limit cycle; (IV) a stable focus; (V) a stable node, a stable focus, and a saddle; and (VI) a stable node, a saddle, an unstable focus, and a stable limit cycle. Typical phase portraits of the system in the marked regions are depicted in the right-hand side of the figure.

transcendental equations

$$f(r_e, v_e) = 0, \tag{25a}$$

$$g(r_e, v_e) = 0. \tag{25b}$$

Generally, the closed-form solutions of these equations are not available, but the local bifurcation curves in the plane of parameters $(\bar{\eta}, J)$ can be derived analytically in a parametric form.

A. Saddle-node bifurcation

Saddle-node (SN) bifurcation occurs when two fixed points of a dynamical system collide and annihilate each other. This bifurcation is defined by the condition

$$\det[A(r_e, v_e)] = 0, \tag{26}$$

where $A(r_e, v_e)$ is the Jacobian of the system (22) evaluated at a fixed point. Combining Eqs. (25) and (26), the following parametric equations for the SN bifurcation curve in the $(\bar{\eta}, J)$ plane can be derived as follows:

$$J_{\text{SN}} = \frac{2\left(v_e^2 + r_e^2\pi^2\right)\left[(V_{\text{th}} - v_e)^2 + r_e^2\pi^2\right]}{V_{\text{th}} r_e (V_{\text{th}} - 2v_e)}, \tag{27a}$$

$$\bar{\eta}_{\text{SN}} = \pi^2 r_e^2 - v_e^2 - J_{\text{SN}} V_{\text{th}} S, \tag{27b}$$

where $v_e = -1/(2\pi r_e)$ and the varying parameter is r_e. The variable S is defined by Eq. (20) in which r and v have to be substituted by r_e and v_e, respectively. For the fixed $V_{\text{th}} = 50$, the SN bifurcation is depicted in Fig. 2 by a blue solid curve. The curve has two branches. The point where these branches coalesce corresponds to the cusp (CP) bifurcation. Here the both eigenvalues of the Jacobian matrix vanish.

B. Andronov-Hopf bifurcation

For the two-dimensional system (22), the Andronov-Hopf (AH) bifurcation is defined by two conditions:

$$\text{tr}[A(r_e, v_e)] = 0, \tag{28a}$$

$$\det[A(r_e, v_e)] > 0. \tag{28b}$$

Combining Eqs. (25) with (28a) and taking into account condition (28b), we can again derive parametric expressions for the AH bifurcation curve in the $(\bar{\eta}, J)$ parameter plane:

$$J_H = \frac{-4v_e[(V_{\text{th}} - v_e)^2 + (\pi r_e)^2]}{V_{\text{th}} r_e}, \tag{29a}$$

$$\bar{\eta}_H = \pi^2 r_e^2 - v_e^2 - J_H V_{\text{th}} S, \tag{29b}$$

with $v_e = -1/(2\pi r_e)$ and r_e being the varying parameter. The variable S is defined in the same way as in Eq. (27b). In Fig. 2, the AH bifurcation at $V_{\text{th}} = 50$ is presented by a red dashed curve. This curve joins with the SN curve at the Bogdanov-Takens (BT) bifurcation point.

The region above the AH curve is characterized by the presence of the limit cycle. Since for $V_{\text{th}} \to \infty$ the model (22) transforms into the model of Ref. [24] that does not possess self-oscillations, it is interesting to analyze how the limit-cycle oscillations disappear with the increase of V_{th}. To this end, in Fig. 3 we plot a family of AH curves for different values of the parameter V_{th}. We see that these curves rise in the $(\bar{\eta}, J)$ plane when the parameter V_{th} is increased. This means that the threshold value of the coupling strength J that provides self-oscillations increases with the increase of V_{th} and the self-oscillations become impossible for any finite J and $\bar{\eta}$ when $V_{\text{th}} \to \infty$.

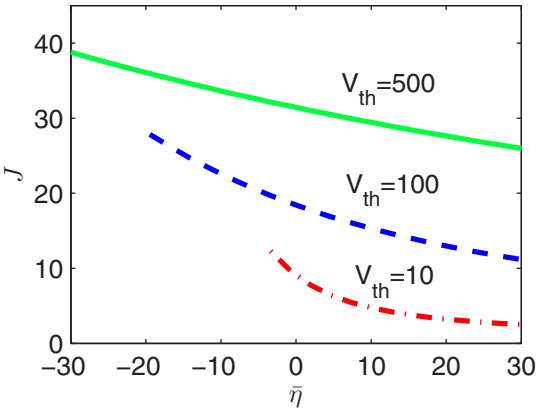

FIG. 3. An evolution of the Androv-Hopf bifurcation curve in the $(\bar{\eta}, J)$ plane with the increase of the threshold voltage V_{th}.

C. Homoclinic bifurcation

The homoclinic bifurcation (HB) is a global bifurcation and in this case it cannot be specified analytically. The curve representing the homoclinic bifurcation is shown in Fig. 2 by green connected points. It was estimated numerically by using the shooting method [38]. The HB curve starts from the Bogdanov-Takens point and then approaches the right-hand-side branch of the SN curve.

D. Comparison of bifurcations in the macroscopic and microscopic models

In order to verify how well the macroscopic model (22) predicts the above bifurcations in the microscopic system (23), in Fig. 4 we plot the asymptotic values of the synaptic variable S (multiplied by V_{th}) as a function of the parameter $\bar{\eta}$ computed from both the macroscopic and microscopic models. These diagrams are presented for the fixed value of the threshold voltage $V_{\text{th}} = 50$ and different values of the coupling strength J. The curves represent the results derived from the macroscopic model by the continuation method, while the symbols show the results obtained by numerical simulation of the microscopic equations. In all cases a good agreement between both results is observed.

The saddle-node bifurcation appears in Figs. 4(a) and 4(c) at those values of $\bar{\eta}$ where the red solid curve representing a stable fixed point merges with the blue dashed curve that corresponds to an unstable fixed point. In Fig. 4(b), the SN bifurcation appears as a collision and annihilation of two unstable fixed points. The Andronov-Hopf bifurcation occurs in Figs. 4(a) and 4(c) where the red solid curve branches into three curves: a blue dashed curve and two solid green (light) curves. The latter two curves indicate the maximal and minimal values of the oscillating variable $S(t)V_{\text{th}}$. The homoclinic bifurcation is seen in Fig. 4(b). For large $\bar{\eta}$, the only attractor in the system is the limit cycle. When the parameter $\bar{\eta}$ is decreased, the limit cycle collides with an unstable fixed point and the oscillations suddenly disappear. Then the only stable steady-state solution with low synaptic activity remains in the system. Note that in Figs. 4(a) and 4(c), there are bistabilities at certain intervals of the parameter $\bar{\eta}$. In Fig. 4(a) a stable limit cycle coexists with a stable fixed point, while in Fig. 4(c) two stable fixed points coexist.

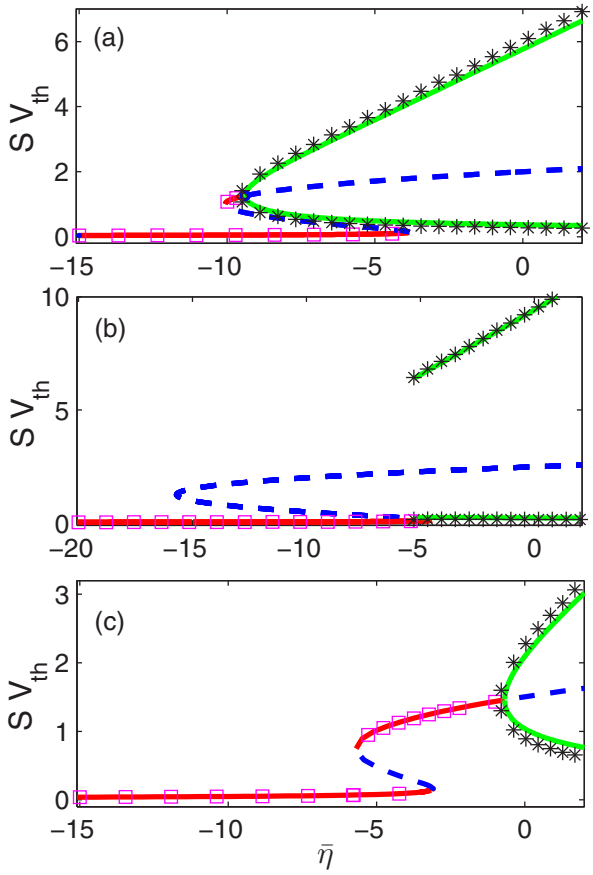

FIG. 4. Asymptotic values of the synaptic variable S multiplied by V_{th} as a function of the parameter $\bar{\eta}$. The red solid curve represents the stable fixed points, the blue dashed curve shows unstable fixed points, and the green (light) solid curve denote the minimal and maximal values of the periodically oscillating variable $S(t)V_{\text{th}}$. The curves are derived from the macroscopic model (22), while the symbols show the results obtained from numerical simulations of QIF neurons. Squares denote the averaged stationary values of SV_{th}, while the asterisks the averaged minimal and maximal values of the oscillating variable $S(t)V_{\text{th}}$. Parameters are $N = 10\,000$, $V_{\text{th}} = 50$, (a) $J = 25$, (b) $J = 20$, and (c) $J = 15$.

V. AGING TRANSITION

One of the most important problems about a large population of coupled neurons is how robust its macroscopic activity is against various types of local damage or deterioration such that some neurons become nonspiking. When the proportion p of the inactive neurons is progressively increased, the amplitude of global oscillations decreases and vanishes at some critical value p_c. This phenomenon is termed the *aging transition*. The parameter p_c varies in the interval $[0,1]$ and serves as a measure for the robustness against aging. The larger the p_c the more robust the system is to neurons' inactivation damage.

Here we analyze the aging effects in a model described by microscopic Eqs. (23) and macroscopic Eqs. (22). We are

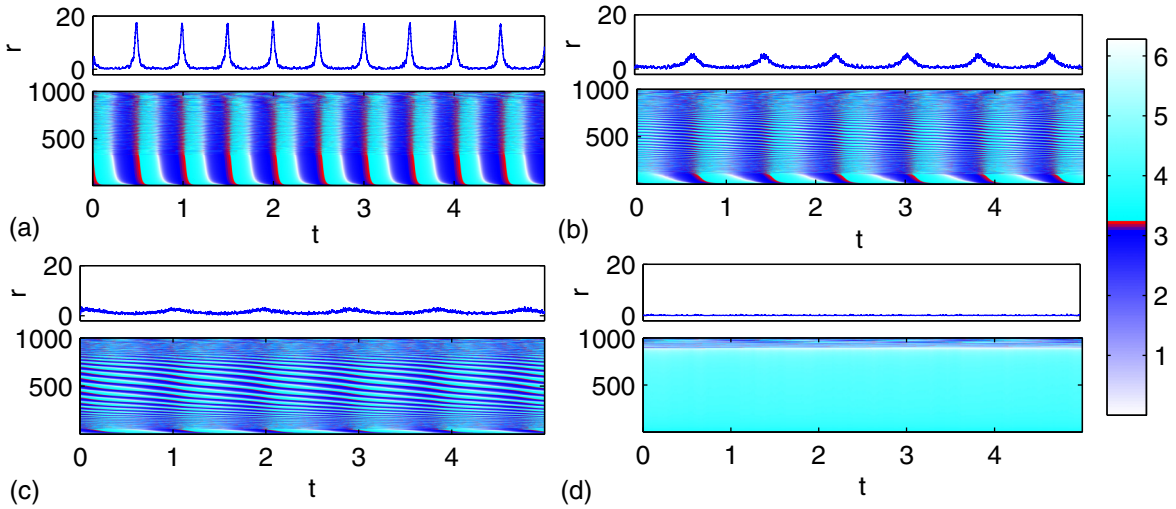

FIG. 5. Dynamics of the firing rate r (top graphics in each panel) and the phases θ_j presented by colors (bottom graphics in each panel) of $N = 1000$ synaptically coupled QIF neurons. Parameters are $V_{\rm th} = 50$, $J = 15$, (a) $p = 0.01$ ($\bar{\eta} = 31.82$), (b) $p = 0.05$ ($\bar{\eta} = 6.31$), (c) $p = 0.3$ ($\bar{\eta} = 0.73$), and (d) $p = 0.92$ ($\bar{\eta} = -3.89$).

particularly interested in how the aging transition depends on the coupling strength and the width of synaptic pulses. In our network, the bifurcation parameter that subdivides the free neurons into active and inactive ones is η. The neurons with $\eta < 0$ are inactive; for $J = 0$ they are in an excitable regime. The neurons with $\eta > 0$ are active; for $J = 0$ they generate periodical spikes. If the parameter η satisfies the Lorentzian distribution (18), then the proportion of inactive neurons is

$$p = \frac{1}{2} - \frac{1}{\pi}\arctan(\bar{\eta}). \tag{30}$$

Recall that the width of the Lorentzian is assumed to be $\Delta = 1$. Thus the value of p is uniquely defined by the center $\bar{\eta}$ of the Lorentzian distribution. The proportion p of inactive neurons is monotonically decreased from 1 to 0 when $\bar{\eta}$ is increased from $-\infty$ to $+\infty$. When $\bar{\eta} = 0$ the parameter p is equal to $1/2$.

In Fig. 5, we show how the aging transition manifests itself for the QIF neurons on both the microscopic and macroscopic levels. In each panel of this figure, the curves show the macroscopic dynamics of the firing rate (top graphics), while the colored (bottom) graphics represent the dynamics of the phases θ_j of particular neurons. The phases θ_j are related with the voltages V_j as $V_j = \tan(\theta_j/2)$. At the spike moment of the jth neuron, its voltage approaches infinity, $V_j \to \infty$, which corresponds to the phase $\theta_j \to \pi$. In all panels, we fix the coupling strength and the threshold voltage and vary only the parameter p by changing $\bar{\eta}$. In Fig. 5(a), almost all neurons are active; the proportion of inactive neurons is only $p = 0.01$. Due to synaptic coupling, most active neurons synchronize and produce large-amplitude oscillations of the firing rate. In Figs. 5(b) and 5(c), the proportion of inactive neurons is increased to $p = 0.05$ and $p = 0.3$, respectively. The coherence of neurons decreases and this causes the decrease of the firing rate oscillation amplitude. Finally, when the parameter p exceeds some critical value, the firing rate ceases to oscillate. This is demonstrated in Fig. 5(d) for $p = 0.92$. Here, almost all neurons are quenched into the excitable state and the small amount of incoherently spiking neurons cannot force the inactive neurons to produce spikes.

Note that the macroscopic oscillations of the firing rate occur only when almost all neurons, including those that are inactive without coupling, produce spikes. Thus, it is interesting to analyze how the coupling influences the proportion P of inactive neurons. We denote the proportion of inactive neurons in the coupled network by the capital letter P in order to distinguish it from the proportion p of inactive neurons in the absence of coupling. Obviously, for $J = 0$ these definitions coincide, $P = p$. When there are no macroscopic oscillations, the value P can be estimated analytically. In this case, the synaptic variable $S(t) = S$ as well as the density $\rho(V|\eta,t) = \rho(V|\eta)$ are independent of time and the proportion of spiking neurons $R = 1 - P$ can be found from the integral

$$R = \int_{-\infty}^{+\infty}\int_{\eta_c}^{+\infty} \rho(V|\eta)g(\eta)d\eta dV. \tag{31}$$

Here $\eta_c = -JV_{\rm th}S$ is the critical value of the parameter η that subdivides the interacting neurons into spiking ($\eta > \eta_c$) and nonspiking ($\eta < \eta_c$) ones.

In order to estimate the stationary density $\rho(V|\eta)$, we need to find the stationary solutions of Eqs. (24) and substitute them into Eq. (9). The stationary solution of Eqs. (24) for spiking neurons that satisfy the inequality $\eta > -JV_{\rm th}S$ is $y(\eta,t) = 0$ and $x(\eta,t) = \sqrt{JV_{\rm th}S + \eta}$. Thus the stationary density for $\eta > \eta_c$ reads

$$\rho(V|\eta) = \frac{1}{\pi}\frac{\sqrt{JV_{\rm th}S + \eta}}{V^2 + JV_{\rm th}S + \eta}. \tag{32}$$

Substituting Eqs. (18) and (32) into Eq. (31) and solving the integrals, we obtain the following expression for $P = 1 - R$:

$$P = \frac{1}{2} - \frac{1}{\pi}\arctan(JV_{\rm th}S + \bar{\eta}). \tag{33}$$

The parametric dependence of P on J can be obtained by expressing J from the equilibrium conditions (25) of the

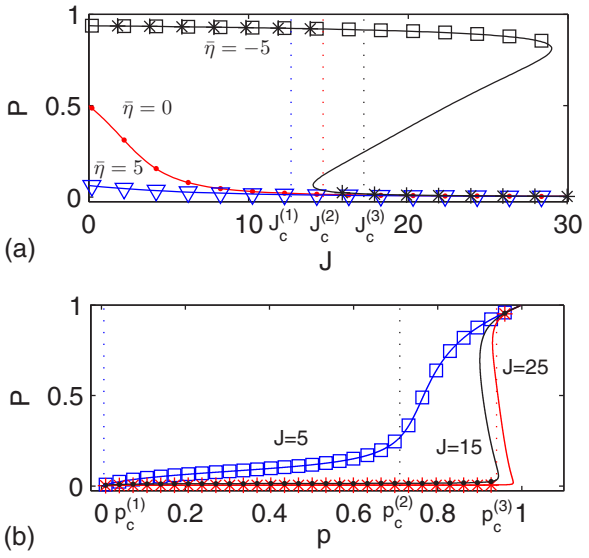

FIG. 6. (a) The proportion P of inactive neurons in the coupled network as a function of the coupling strength J for different values of the parameter $\bar{\eta}$. Solid curves represent analytical results obtained from Eqs. (33) and (34), while the symbols show the results of numerical simulation of the microscopic model with $N = 10\,000$ neurons. The squares and asterisks for $\bar{\eta} = -5$ correspond to the increase and decrease of the coupling strength, respectively. The vertical dotted lines indicate the onset of macroscopic oscillations. They correspond to the following values of the coupling strength: $J_c^{(1)} = 12.67$ ($\bar{\eta} = 5$), $J_c^{(2)} = 14.68$ ($\bar{\eta} = 0$), and $J_c^{(3)} = 17.22$ ($\bar{\eta} = -5$). The threshold voltage is $V_{\text{th}} = 50$. (b) The proportion P of inactive neurons in the coupled network as a function of the proportion p of inactive neurons in the absence of coupling for different values of the coupling strength J. Solid curves show analytical results obtained from Eqs. (33) and (34), while the symbols correspond to numerical simulation of the microscopic model. The vertical dotted lines indicate the critical values p_c at which the oscillations cease to exist: $p_c^{(1)} = 0.006$ ($J = 5$), $p_c^{(2)} = 0.71$ ($J = 15$), and $p_c^{(3)} = 0.94$ ($J = 25$).

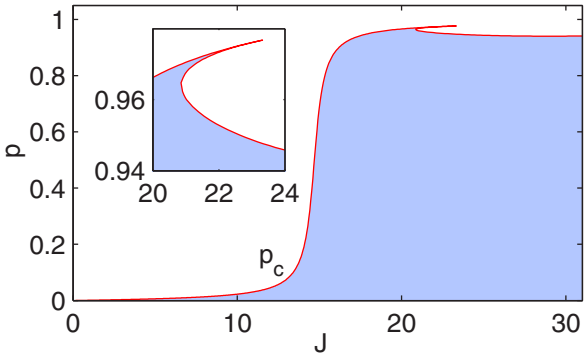

FIG. 7. Bifurcation diagram in the (J, p) plane. The colored region corresponds to macroscopic oscillations of the firing rate and the mean membrane potential. The border of this region depicted by the red solid curve defines the dependence of the robustness parameter p_c on the coupling strength J. The inset shows an enlarged region of the main figure. The threshold voltage is $V_{\text{th}} = 50$.

reduced system (22),

$$J = -\frac{\bar{\eta} + v_e^2 - \pi^2 r_e^2}{V_{\text{th}} S}. \tag{34}$$

The desired dependence is defined by Eqs. (33) and (34), where $v_e = -1/(2\pi r_e)$ and the varying parameter is r_e. The variable S is defined by Eq. (20) in which r and v have to be substituted by r_e and v_e, respectively. In Fig. 6(a), this dependence is plotted by solid curves for the fixed V_{th} and different values of $\bar{\eta}$. The dependence is in good agreement with the results of direct numerical simulation of the microscopic Eqs. (23) shown in the figure by symbols. We see that the increase of the coupling strength leads to the decrease of the proportion of inactive neurons and the macroscopic oscillations appear when almost all neurons become active. The critical values of the coupling J_c at which the macroscopic oscillations appear through Hopf bifurcation are numerically estimated from Fig. 2 and marked in the figure by vertical dotted lines.

When the initial proportion p of inactive neurons is large (for $\bar{\eta} = -5$), then there is a bistability in a certain interval of the coupling strength J, where the macroscopic oscillations coexist with the stationary state. Numerical simulation of the microscopic Eqs. (22) in this case shows a hysteresis when gradually increasing and decreasing the coupling strength.

In Fig. 6(b), we show how the proportion P of inactive neurons in the coupled network changes when varying the parameter $\bar{\eta}$ that governs the proportion p of inactive neurons in the absence of coupling. The parametric dependence of P on p is defined by Eqs. (30) and (33) in which the parameter $\bar{\eta}$ has to be extracted from the equilibrium conditions (25) of the system (22), $\bar{\eta} = \pi^2 r_e^2 - v_e^2 - J V_{\text{th}} S$. Again, the dependence of P on p obtained by direct numerical simulations of the microscopic Eqs. (22) shows a good agreement with the results derived from Eqs. (30) and (33). We see that for sufficiently large values of the coupling strength J, the increase of the proportion p of inactive neurons in an uncoupled network almost does not influence the proportion P of inactive neurons in the coupled network. The proportion P remains small even for sufficiently large values of p. Thus, the robustness of the system against aging is provided by the fact that most of the coupled neurons remain active with the increase of p. The critical values p_c at which the oscillations cease to exist are numerically estimated from the bifurcation diagram in Fig. 2 in a way similar to the critical values J_c. They are marked in Fig. 6 by the vertical dotted lines. We see that for $J = 15$ and $J = 25$ the oscillations maintain when p is increased up to the values $p_c = 0.71$ and $p_c = 0.94$, respectively.

The dependence of the robustness criterion p_c on the coupling strength J is shown in Fig. 7. The colored region in the plane of the parameters (J, p) corresponds to the presence of macroscopic oscillations of the firing rate and the mean membrane potential. The border of this region depicted by the red solid curve defines the dependence of the robustness p_c on the coupling strength J. When the coupling strength exceeds some defined value (for the given values of the parameters it is $J \approx 15$), the system becomes very robust against aging with the parameter p_c close to 1. The high level of the robustness remains almost unchanged with the further increase of the coupling strength.

The complex dependence of the robustness in the interval $20 < J < 24$ is related to the bistability. This region is enlarged in the inset. In the upper narrow part of this region, the

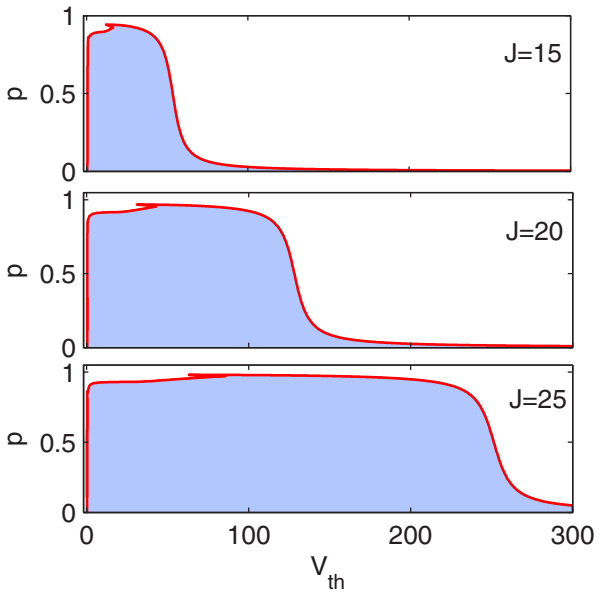

FIG. 8. Bifurcation diagrams in the $(V_{\rm th}, p)$ plane for different values of the coupling strength J. In the colored regions, there are macroscopic oscillations. The borders of the regions depicted by the red solid curves define the dependence of the parameter p_c on the threshold voltage $V_{\rm th}$.

system may either demonstrate macroscopic oscillations or be in the stable stationary state. Interestingly, here the system may show a counterintuitive response to the variation of parameter p. Suppose that the parameters are taken from the upper narrow part of the diagram and the initial conditions are chosen such that the system demonstrates macroscopic oscillations. Then the decrease of p, i.e., the increase of the proportion of spiking neurons, will lead to a sudden cease of oscillations.

Finally, in Fig. 8, we show the dependence of the robustness p_c on the threshold voltage $V_{\rm th}$, which is inversely proportional to the width of synaptic pulses. The colored regions in the plain of the parameters $(V_{\rm th}, p)$ again correspond to the presence of macroscopic oscillations and the border curves represent the robustness p_c. As seen from the figure, the system is robust against aging when the value of $V_{\rm th}$ lies in a certain interval. The larger the coupling strength J the wider the interval. Remarkably, the robustness p_c is close to 1 and is almost independent of the specific value of $V_{\rm th}$ (and thus of the specific width of synaptic pulses) provided it is chosen from the given interval.

Generalizing the results presented in Figs. 7 and 8, one can conclude that the macroscopic oscillations in the heterogeneous network of synaptically coupled QIF neurons are highly robust against aging damage provided the coupling strength and the width of synaptic pulses are sufficiently large. The global synchronous oscillations are preserved even when the most part of spiking neurons transforms into excitable neurons.

VI. DISCUSSION

We have analyzed a heterogeneous network of all-to-all coupled quadratic integrate-and-fire neurons with a synaptic interaction that takes into account the finite width of synaptic pulses. The network contains a mixture of at-rest but excitable neurons as well as spontaneously spiking neurons. Applying a recently developed reduction technique based on the Lorentzian ansatz [24], we have derived the closed system of macroscopic equations for the neuron's firing rate and mean membrane potential, which are exact in the thermodynamic limit. The bifurcation analysis of these equations revealed a rich scenario of the asymptotic behavior, including two stable equilibrium states with low and high time-independent spiking rate and the periodic limit-cycle oscillations of the firing rate and the mean membrane potential. The system may also demonstrate bistabilities that coexist with either two stable equilibrium states or a stable limit cycle and a stable equilibrium state. We have found that the finite width of synaptic pulses is a necessary ingredient for the appearance of macroscopic self-oscillations. In the simplified model [24], where synaptic pulses are approximated by the Dirac δ function, such oscillations do not exist.

The reduced system of macroscopic equations is useful to analyze an aging transition in the network, i.e., the robustness of the macroscopic self-oscillation against damage that increases the proportion of inactive neurons in the network. By investigating the dependence of the aging transition on the strength of synaptic coupling and the width of synaptic pulses, we have established that the network is highly robust against aging damage provided the latter two parameters are sufficiently large. The macroscopic self-oscillations persist even when most of the inherently spiking neurons turn into excitable neurons.

The results obtained from the reduced equations, including the analytically determined bifurcation curves, are in excellent agreement with the results of direct numerical simulations of the microscopic equations, when the total number of neurons in the network is about 10 000; a good agreement is obtained even for networks composed of only 1000 neurons. Thus the reduced model predicts well the behavior of finite-size networks and allows us to better understand the properties, functions, and robustness of real networks composed of active and inactive units like neurons in the brain or heart cells.

ACKNOWLEDGMENT

This work was supported by Grant No. MIP-15040/2015 of the Research Council of Lithuania.

APPENDIX A: NUMERICAL SIMULATIONS

Direct numerical integration of microscopic model Eq. (6) or Eq. (23) is problematic because the membrane potential of the QIF neuron tends to infinity at the moment when the neuron fires. This problem can be avoided by the change of variables

$$V_j = \tan(\theta_j/2) \tag{A1}$$

that transforms the QIF neurons into theta neurons, where θ_j is the phase of the jth neuron. Then the model (6) in the theta representation reads:

$$\dot{\theta}_j = (1-\cos\theta_j) + (1+\cos\theta_j)[\eta_j + K V_s S(t)] - K\sin(\theta_j) S(t). \tag{A2}$$

The synaptic variable $S(t)$ is defined by Eq. (5) and the substitution (A1). When the QIF neuron fires, its membrane

potential approaches infinity, $V_j \to \infty$, and then its value is reset to minus infinity, $V_j \to -\infty$. In the theta representation, this means that the phase θ_j simply crosses the value π. The system (23) in the theta representation reads:

$$\dot{\theta}_j = (1 - \cos\theta_j) + (1 + \cos\theta_j)[\eta_j + J V_{\text{th}} S(t)]. \quad \text{(A3)}$$

Thus, instead of simulating Eqs. (6) and (23) for the QIF neurons, we performed numerical simulations of the equivalent systems of Eqs. (A2) and (A3), respectively, for the theta neurons. The latter equations were integrated by the Euler method with time step $dt = 10^{-4}$. The population of N theta neurons with the Lorentzian distribution Eq. (18) were deterministically generated using $\eta_j = \bar{\eta} + \Delta \tan[(\pi/2)(2j - N - 1)/(N + 1)]$, where $j = 1, \ldots, N$ and $\Delta = 1$. Such a numeration of neurons means that the free neurons with the index $j < j_c = (N + 1)/2 - (2N + 1)\arctan(\bar{\eta})/\pi$ are excitable and the neurons with the index $j > j_c$ are spiking.

At each step of integration of Eqs. (A2) or (A3), the synaptic variable (5) was estimated as $S(t) = dN_s/N$, where dN_s is the number of neurons whose phases are in the interval $\theta \in [2\arctan(V_{\text{th}}), \pi]$. Similarly, the firing rate of Eqs. (A2) was estimated as $r = dN_r/(N dt)$, where dN_r is the number of neurons whose phases are in the interval $\theta \in (\pi - 2dt, \pi)$. This estimation is based on the assumption that the time step dt is small and thus the phase speed of neurons close to the firing phase $\theta = \pi$ can be approximated as $\dot{\theta}_j \approx 2$. Since the quantity dN_r fluctuates in time, the firing rate varies nonsmoothly. In Fig. 5 this function is smoothed by using a moving average with a time window of the size $\delta t = 10^{-2}$.

The initial conditions for the reduced systems Eqs. (21) and (22) were derived from the initial conditions of the theta neurons Eqs. (A2) and (A3) by computing the Kuramoto order parameter

$$Z = \frac{1}{N}\sum_{j=1}^{N} \exp(i\theta_j) \quad \text{(A4)}$$

and using the relation between Z and the firing rate quantity $W \equiv \pi r + iv$:

$$W = \frac{1 - Z^*}{1 + Z^*}, \quad \text{(A5)}$$

where Z^* means complex conjugate of Z (cf. Ref. [24] for more details). Thus the initial values of the firing rate r and the mean membrane potential v can be extracted from the initial distribution of the phases θ_j using Eqs. (A4) and (A5).

APPENDIX B: BIFURCATION DIAGRAM AND THE AGING TRANSITION FOR THE ORIGINAL MODEL

Here we present the bifurcation diagram for the original macroscopic model Eqs. (21), which describes the network of QIF neurons Eqs. (6) with a synaptic coupling that takes into account the finite value of the reversal potential V_s. Unlike the simplified coupling case defined by macroscopic Eqs. (22), here an analytical treatment is impossible. Numerically obtained bifurcation diagram for Eqs. (21) is presented in Fig. 9. The curves of the saddle-node and Andronov-Hopf bifurcations were computed with the help of MatCont package [39], while the curve of the homoclinic bifurcation was estimated by the shooting method [38]. Comparing the bifurcation diagrams presented in Figs. 9 and 2 one can conclude that they are qualitatively similar. Thus the simplified model (22) captures well the main features of the original model (21).

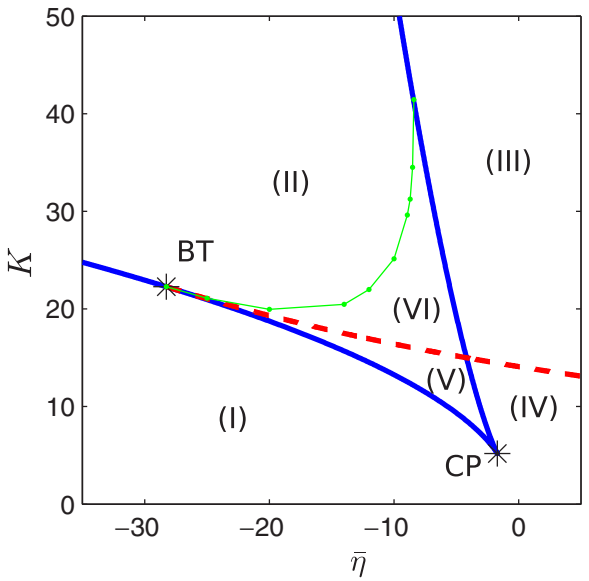

FIG. 9. Two-parameter bifurcation diagram of the macroscopic model (21). The bifurcation in the parameter space $(\bar{\eta}, K)$ for the fixed parameters $V_{\text{th}} = 50$ and $V_s = 75$. All denotations are the same as in Fig. 2.

In addition, in Fig. 10 we show the aging behavior of the original system (21). Comparing this figure with Fig. 7 we see that the qualitative equivalence of the simplified model (22) and the original model (21) is conserved for the aging transition as well. The only difference is here the characteristic curve defining the robustness is shifted to larger values of the coupling strength J.

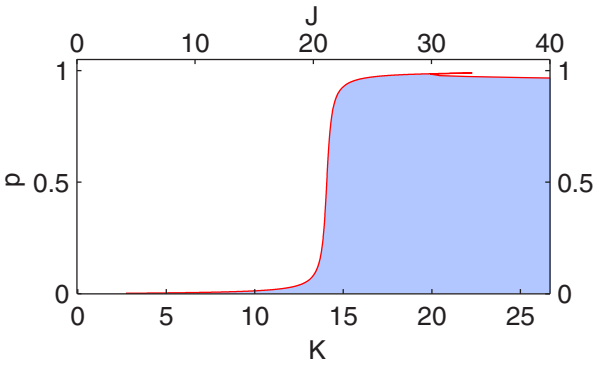

FIG. 10. Bifurcation diagram of the macroscopic model (21) in the (K, p) plane. The upper axis shows the values of the rescaled coupling strength $J = KV_s/V_{\text{th}}$ in order to compare the results with those presented in Fig. 7. The colored region corresponds to macroscopic oscillations of the firing rate and the mean membrane potential. The border of this region depicted by the red solid curve defines the dependence of the robustness parameter p_c on the coupling strength K. All parameters are the same as in Fig. 9.

[1] A. Pikovsky, M. Rosenblum, and J. Kurths, *Synchronization: A Universal Concept in Nonlinear Sciences* (Cambridge University Press, Cambridge, 2001).
[2] S. H. Strogatz, Physica D **143**, 1 (2000).
[3] J. A. Acebrón, L. L. Bonilla, C. J. Pérez Vicente, F. Ritort, and R. Spigler, Rev. Mod. Phys. **77**, 137 (2005).
[4] F. Dörfler and F. Bullo, Automatica **50**, 1539 (2014).
[5] K. Wiesenfeld, P. Colet, and S. H. Strogatz, Phys. Rev. Lett. **76**, 404 (1996).
[6] M. Rohden, A. Sorge, M. Timme, and D. Witthaut, Phys. Rev. Lett. **109**, 064101 (2012).
[7] L. Glass, Nature **410**, 277 (2001).
[8] G. Bard Ermentrout and D. H. Terman, *Mathematical Foundations of Neuroscience* (Springer, New York, 2010).
[9] A. T. Winfree, J. Theor. Biol. **16**, 15 (1967).
[10] Y. Kuramoto, *Lecture Notes in Physics, International Symposium on Mathematical Problems in Theoretical Physics*, edited by H. Araki, Vol. 39 (Springer-Verlag, New York, 1975); *Chemical Oscillations, Waves and Turbulence*, Vol. 39 (Springer-Verlag, New York, 1984).
[11] E. Ott and T. M. Antonsen, Chaos **18**, 037113 (2008).
[12] E. Ott and T. M. Antonsen, Chaos **19**, 023117 (2009).
[13] E. A. Martens, E. Barreto, S. H. Strogatz, E. Ott, P. So, and T. M. Antonsen, Phys. Rev. E **79**, 026204 (2009).
[14] E. Ott, B. R. Hunt, and T. M. Antonsen, Chaos **21**, 025112 (2011).
[15] A. Pikovsky and M. Rosenblum, Physica D **240**, 872 (2011).
[16] H. Hong and S. H. Strogatz, Phys. Rev. Lett. **106**, 054102 (2011).
[17] M. Wolfrum, S. V. Gurevich, and O. E. Omel'chenko, Nonlinearity **29**, 257 (2016).
[18] T. B. Luke, E. Barreto, and P. So, Neur. Comput. **25**, 3207 (2013).
[19] P. So, T. B. Luke, and E. Barreto, Physica D **267**, 16 (2014).
[20] T. B. Luke, E. Barreto, and P. So, Front. Comput. Neurosci. **8**, 1 (2014).
[21] C. R. Laing, Phys. Rev. E **90**, 010901 (2014).
[22] C. R. Laing, SIAM J. Appl. Dynam. Syst. **14**, 1899 (2015).
[23] D. Pazó and E. Montbrió, Phys. Rev. X **4**, 011009 (2014).
[24] E. Montbrió, D. Pazó, and A. Roxin, Phys. Rev. X **5**, 021028 (2015).
[25] H. Daido and K. Nakanishi, Phys. Rev. Lett. **93**, 104101 (2004).
[26] D. Pazó and E. Montbrió, Phys. Rev. E **73**, 055202 (2006).
[27] H. Daido and K. Nakanishi, Phys. Rev. E **75**, 056206 (2007).
[28] H. Daido, Europhys. Lett. **84**, 10002 (2008).
[29] H. Daido, A. Kasama, and K. Nishio, Phys. Rev. E **88**, 052907 (2013).
[30] G. Tanaka, K. Morino, H. Daido, and K. Aihara, Phys. Rev. E **89**, 052906 (2014).
[31] B. Thakur, D. Sharma, and A. Sen, Phys. Rev. E **90**, 042904 (2014).
[32] M. C. Antle, D. K. Foley, N. Foley, and R. Silver, J. Biol. Rhythms **18**, 339 (2003).
[33] S. J. Aton and E. D. Herzog, Neuron **48**, 531 (2005).
[34] E. Miake, J. Marbán, and H. B. Nuss, Nature **419**, 132 (2002).
[35] Y. Hu, J. F. Dawkins, H. C. Cho, E. Marbán, and E. Cingolani, Sci. Transl. Med. **6**, 245ra94 (2014).
[36] J. Sneyd, ed., *Proceedings of Symposia in Applied Mathematics*, Vol. 59 (American Mathematical Society, Providence, Rhode Island, 2002).
[37] A. Roth and M. C. W. van Rossum, in *Computational Modeling Methods for Neuroscientists*, edited by E. D. Schutter (The MIT Press, Cambridge, London, 2009), Chap. 6, pp. 139–159.
[38] A. C. Scott, *Neuroscience: A Mathematical Primer* (Springer, New York, 2002).
[39] A. Dhooge, W. Govaerts, and Y. A. Kuznetsov, ACM Trans. Math. Softw. **29**, 141 (2003).